

Flexible high-entropy functional ceramics

Received: 5 November 2024

Accepted: 27 May 2025

Published online: 01 July 2025

Check for updates

Lvye Dou^{1,2,16}, Bingbing Yang^{1,3,16}, Xiaoyuan Ye^{4,16}, Yang Zhang^{5,6}, Wenqing Zhu^{7,8}, Huiling Chen⁴, Yingjie Jiang⁷, Ben Fang⁷, Shun Lan¹, Qian Li¹, Yiqian Liu¹, Penghui Li^{9,10}, Xuan Zhang¹¹, Shuchang Li¹², Yujun Zhang¹³, Wei Xu¹³, Xinyu Zhang¹⁴, Liang Wu¹⁴, Xiaoyan Li¹², Xiaoding Wei^{7,15}✉, Zhiyang Yu⁴✉, Ce-Wen Nan¹ & Yuan-Hua Lin¹✉

Functional ceramics, once integrated with flexibility, hold great promise for cutting-edge electronic devices. Unfortunately, functionality and flexibility are inherently exclusive in ceramics: the long-range order of ionic lattices bestows polarization-like properties that accompany brittleness, whereas disorder tolerates bond rotation to generate flexibility with significant loss of performance. Implanting ordered functional motifs within amorphous ceramics, though challenging, may balance this trade-off. Here, the challenge is met through a high-entropy strategy, which allows the initial crystallization of randomly dispersed nanocrystals followed by controlled amorphization of high-entropy compositions to attain a crystalline/amorphous microstructure, yielding a $\text{Bi}_4\text{Ti}_3\text{O}_{12}$ -based film that can withstand $\sim 180^\circ$ folding with a bending strain and tensile elongation up to 4.80% and 5.29%, respectively. The crystalline/amorphous structure enables the production of a flexible dielectric capacitor with high permittivity (~ 35), good temperature stability and durability. This strategy offers research prototypes for customizing the microstructures of functional ceramics, advancing next-generation ceramics with flexibility.

Functional ceramic materials, represented by a large family of complex crystalline oxides, feature fascinating physical (electronic, magnetic, acoustic, optical, and coupling thereof) properties^{1–3} and constitute important components in modern high-tech fields such as electronic information^{4,5}, flexible displays^{6,7}, and energy technology^{8,9}. Over the

past few decades, the blooming of wearable and stretchable electronic devices has spurred an urgent demand for integrating functional ceramics with high flexibility, the combination of which advances the miniaturization and integration of high-tech information technology¹⁰. The prevailing approach presently involves coating stiff ceramic films

¹State Key Laboratory of New Ceramic Materials, School of Materials Science and Engineering, Tsinghua University, Beijing, China. ²School of Materials Science and Engineering, University of Science and Technology Beijing, Beijing, China. ³Key Laboratory of Materials Physics Institute of Solid State Physics HFIPS, Chinese Academy of Sciences, Hefei, China. ⁴State Key Laboratory of Photocatalysis on Energy and Environment, College of Chemistry, Fuzhou University, Fuzhou, China. ⁵State Key Laboratory of Low Dimensional Quantum Physics and Department of Physics, Tsinghua University, Beijing, China. ⁶Rowland Institute at Harvard, Harvard University, Cambridge, MA, USA. ⁷State Key Laboratory for Turbulence and Complex System, Department of Mechanics and Engineering Science, College of Engineering, Peking University, Beijing, China. ⁸Department of Mechanical Engineering, College of Engineering, City University of Hong Kong, Hong Kong, China. ⁹Center for High Pressure Science, State Key Laboratory of Metastable Materials Science and Technology, Yanshan University, Qinhuangdao, China. ¹⁰Center for X-mechanics, School of Aeronautics and Astronautics, Zhejiang University, Hangzhou, China. ¹¹Department of Advanced Manufacturing and Robotics, College of Engineering, Peking University, Beijing, China. ¹²Mechano-X Institute, Applied Mechanics Laboratory, Department of Engineering Mechanics, Tsinghua University, Beijing, China. ¹³Beijing Synchrotron Radiation Facility, Institute of High Energy Physics, Chinese Academy of Sciences, Beijing, China. ¹⁴Faculty of Materials Science and Engineering, Kunming University of Science and Technology, Kunming, China. ¹⁵Peking University Nanchang Innovation Institute, Nanchang, China. ¹⁶These authors contributed equally: Lvye Dou, Bingbing Yang, Xiaoyuan Ye. ✉e-mail: xdwei@pku.edu.cn; yuzyemlab@fzu.edu.cn; linyeh@tsinghua.edu.cn

on flexible substrates, with efforts on developing compatible supporting layers (e.g., polymers, metal foils, or mica)^{11–13}. Nevertheless, the intrinsic brittleness of functional ceramic materials persists in causing potential failures of devices¹⁴, thus posing a major challenge for developing functional-ceramic-based devices.

Flexibility is the mechanical response of a material, measured by its capacity to distribute the external stress evenly within its constitutional structural units in a recoverable manner when subjected to deformation. The key to achieving high flexibility/ductility in ceramics thus lies in their structural design. Major progress has been made in structural ceramics, where a vast of design approaches have been devised to manipulate the structural parameters of materials over multiple scales, including three-dimensional interlocked architecture¹⁵, double-paned hyperbolic structure¹⁶, octet-truss nanolattice design¹⁷, devising fine-grained nanofibers^{18,19}, construction of coherent or semi-coherent interfaces^{20–22}, and creation of hypocrySTALLINE dual phases²³, etc. For designing functional ceramics, a critical but frequently overlooked parameter is the structural order of materials that are often described as crystallinity^{24,25}. On one hand, a long-range lattice order contributes to excellent functionality, such as collective polarization underlying dielectric and ferroelectric performance²⁶, whilst the rigidity of ionic lattices, associated with strong directional bonds and the charge neutrality requirement during deformation, imposes significantly elevated barriers for dislocation movement and thus lowers ductility as opposed to metals and covalently-bonded ceramics²⁷. The accompanying brittleness and inflexibility have become a long-standing obstacle in functional ceramics, with limited progress achieved via specific approaches, such as an extreme reduction in film-thickness²⁸ and exquisitely designed domain structures^{29,30}. On the other hand, disordered motifs can bring forth flexibility or toughness by allowing a certain range of bond rotation/switching^{19,23,31,32}, but they are largely ignored in functional ceramics due to a considerable trade-off between functionality and flexibility. As a consequence, flexibility and functionality are mutually exclusive in functional ceramics, obstructing the production of flexible and stretchable devices.

The significance of structural order enlightens us to seek a new paradigm beyond the conventional research framework that allows the attainment of flexibility from crystalline functional ceramics. A practical strategy is to tune the undulation of structural order within a single ceramic base, where ordered motifs (e.g., crystallized grain) are homogeneously embraced by disordered structural units (e.g., amorphous matrix) at nanoscales. These ideal mosaic microstructures feature the combination of two structural components, an amorphous matrix generating flexibility and its confined nanocrystals contributing to functionality. The key to forming this mosaic structure relies on a controlled crystallization intervention mechanism that continuously occurs throughout a ceramic base, i.e., allowing a first-step crystallization of discrete nano-seeds and then followed with an effective intervention to achieve amorphization till a desired crystalline/amorphous microstructure is modulated. An effective intervention to an initialized crystallization is often seen as a complex task in metals^{33,34}, yet it is less recognized that the regulation may be more straightforward in oxide systems. The reason lies in the fact that, when a complex oxide contains two or more alkali ions in near-equimolar, the diffusivity of the system decreases markedly compared to a single component oxide (known as mixed-alkali effect³⁵). Capitalizing on this decrease can curb a progressive crystallization trend toward amorphization.

Here, in light of the critical effect of multiple-ion-mixing on a controlled crystallization intervention, and affected by the seminal work about entropy-stabilized oxides³⁶, a high-entropy (HE) engineering route therein is proposed to intervene in the crystallization process of functional ceramics: spontaneous compositional fluctuation is utilized to induce the separation of two inter-penetrating

nanophases within a homogeneous high-entropy ceramic base, which develops into a one composition with a preference to crystallize and a high-entropy counterpart stabilizing at amorphous stages due to its sluggish crystallization kinetics. This simple and reproducible protocol, if possible, offers a good opportunity to tailor the microstructure of functional ceramics in a modulated fashion, with great versatility in forming interconnected structures that alternate in structural order (order *vs* disorder) throughout a single ceramic base. In this work, Bi₄Ti₃O₁₂-based dielectric film that can withstand ~180° folding with a bending strain and tensile elongation up to 4.80% and 5.29% was developed through high-entropy strategy. In that way, the HE-engineering strategy paves a new route to integrate flexible structural units as well as mechanical properties in the field of functional ceramics.

Finely modulated crystalline/amorphous microstructure attained by HE-engineering

Functional ceramics are often composed of single-component metal oxides with a strong tendency towards crystallization¹, and thus the stability of amorphous phases containing multiple ions is a primary concern to the implementation of a controlled crystallization intervention. *Ab initio* molecular dynamics (AIMD) simulations were first performed to predict the effect of HE-engineering on the formation of amorphous phases within a series of entropy-modulated Bi_{4-4x}(La, Nd, Pr, Sm)_xTi₃O₁₂ films (molar ratio $x = 0.00, 0.25, 0.50, \text{ and } 0.75$, abbreviated as BiTO films). The nominal configurational entropy can be expressed as Eq. (1):

$$S_{\text{config}} = -R \left(\left(\sum_{i=1}^N x_i \ln x_i \right)_{\text{cation-site}} + \left(\sum_{j=1}^M x_j \ln x_j \right)_{\text{anion-site}} \right) \quad (1)$$

where R , N (M), and x_i (x_j) are the ideal gas constant, atomic species and contents at the cation (anion) sites, respectively³⁷. For $x = 0.00, 0.25, 0.50$ and 0.75 , S_{config} is calculated as $0R, 0.9R, 1.38R$, and $1.6R$, respectively. Then, thermodynamic calculations of Gibbs free energies, using initialized crystalline Bi_{4-4x}(Ln: equimolar La, Nd, Pr, and Sm)_xTi₃O₁₂ ($x = 0.00, 0.25, 0.50, \text{ and } 0.75$) models and relaxed amorphous counterparts (see “Methods” and Supplementary Fig. 1), were conducted to assess the energy barrier (ΔG) for the formation of amorphous phases (Fig. 1a). The Gibbs free energy of a crystalline BiTO ($x = 0.00$) is comparably lower than that of an amorphous one (Fig. 1a, inset, and Supplementary Fig. 2a), indicating an irrepressible crystallization trend when thermal processing an amorphous structure. As S_{config} is increased to $0.9R$ by substituting Bi with La, Nb, Pr, and Sm ($x = 0.25$), the energies of the two phases reverse and the amorphous phase is stabilized. It suggests the feasibility of introducing amorphous phases in functional ceramics by HE-engineering. Upon increasing the configurational entropy to $1.6R$ ($x = 0.75$), the difference in free energies further expands (Fig. 1a, inset, and Supplementary Fig. 2b). Together, it points towards the effectiveness of HE-engineering on crystallization inhibition, i.e., high entropy enhances the stability of amorphous phases over pure BiTO ceramics in a crystalline form.

This allows us to propose a “HE-engineering strategy” (Fig. 1b) that, starting from a fully amorphous high-entropy film, it is possible to take advantage of compositional fluctuation to induce a leading crystallization of Bi-rich (a higher proportion of Bi as compared to Ln, e.g., Bi: Ln = 1: 2) nanocrystals, while leaving the adjacent high-entropy (e.g., Bi, La, Nd, Pr, and Sm in near equimolar) matrix with a sluggish crystallization tendency staying at amorphous stages. As the fluctuation grows, an evenly mixed high-entropy ceramic will evolve into a finely modulated microstructure comprising different crystallinity: crystallized nanograins are homogeneously segmented by an amorphous skeleton within a single ceramic base.

Following the HE-engineering strategy, BiTO thin films (~400 nm in thickness, Supplementary Fig. 3) with S_{config} of 0R, 0.9R, and 1.6R were fabricated using an exfoliation and transfer method (as detailed in the “Methods”). X-ray diffraction (XRD) characterization of the films reveals evident broadening of diffraction peaks within the 0.9R and 1.6R samples (Fig. 1c), with the expanded view showing a hump-like peak in the 1.6R sample. This is in line with our predictions that HE-engineering of complex oxides can stabilize amorphous phases. Then, their microstructural characters are investigated by scanning transmission electron microscopy (STEM). Both 0R and 0.9R samples show polycrystalline microstructures (Fig. 1d, e). The former consists of large grains (~100 nm), with heavy porosities decorating grain boundaries (GBs, Supplementary Fig. 4). The latter has reduced grain sizes with GBs partitioned by amorphous films (~20 nm in thickness, Supplementary Fig. 5), suggesting the emergence of disordered phases at the last stage of crystallization. In contrast, a major morphology change occurs in the BiTO-1.6R sample, chiefly revealing a nanoscale variation in bright and dark contrast. Bright nanopatches (yellow circles, ~2 nm) are partitioned by adjacent dark-contrast nanophases (blue circles, Fig. 1d), forming a distinctly modulated microstructure.

Moreover, electron diffraction analysis was conducted to evaluate the crystallinity within HE-engineered BiTO samples (Fig. 1f). For comparison purposes, all the analyzed diffraction patterns were

obtained from circular regions with a radius of 100 nm. Sharp (117) diffraction spots with a small full width at half maximum (FWHM) of 0.44 nm^{-1} are observed in the BiTO-0R sample (Fig. 1g), again indicating its high crystallinity. The pattern from the BiTO-0.9R sample contains both sharp diffraction spots and diffuse halos around the {117} circle, with a relatively larger FWHM (0.51 nm^{-1}). The halos mainly result from a small fraction of amorphous films situating between crystalline grains. The FWHM of the {117} halos of the BiTO-1.6R sample further increases to 0.65 nm^{-1} , which indicates a substantial increase in the content of amorphous phases.

The phase crystallinity was further probed by nano-beam four-dimensional scanning transmission electron microscopy (4D-STEM) measurements (details shown in Supplementary Fig. 6 and “Methods”). An integrated nano-beam electron diffraction (NBED) pattern, averaged over a rectangular region ($25 \times 25 \text{ nm}^2$) exhibits similar diffuse characters as compared to conventional selected area electron diffraction (Fig. 1h and Supplementary Fig. 7). Narrowing the diffracting region to a bright region ($3 \times 3 \text{ nm}^2$) eventually reveals a certain number of crystalline diffraction spots whilst the concomitant halo comes from the adjoining amorphous matrix (Fig. 1h and Supplementary Fig. 8). The interconnected nanophases in the high-angle annular dark-field (HAADF) images could be assigned as fine nanocrystals segmented by an amorphous matrix, as eventually substantiated by

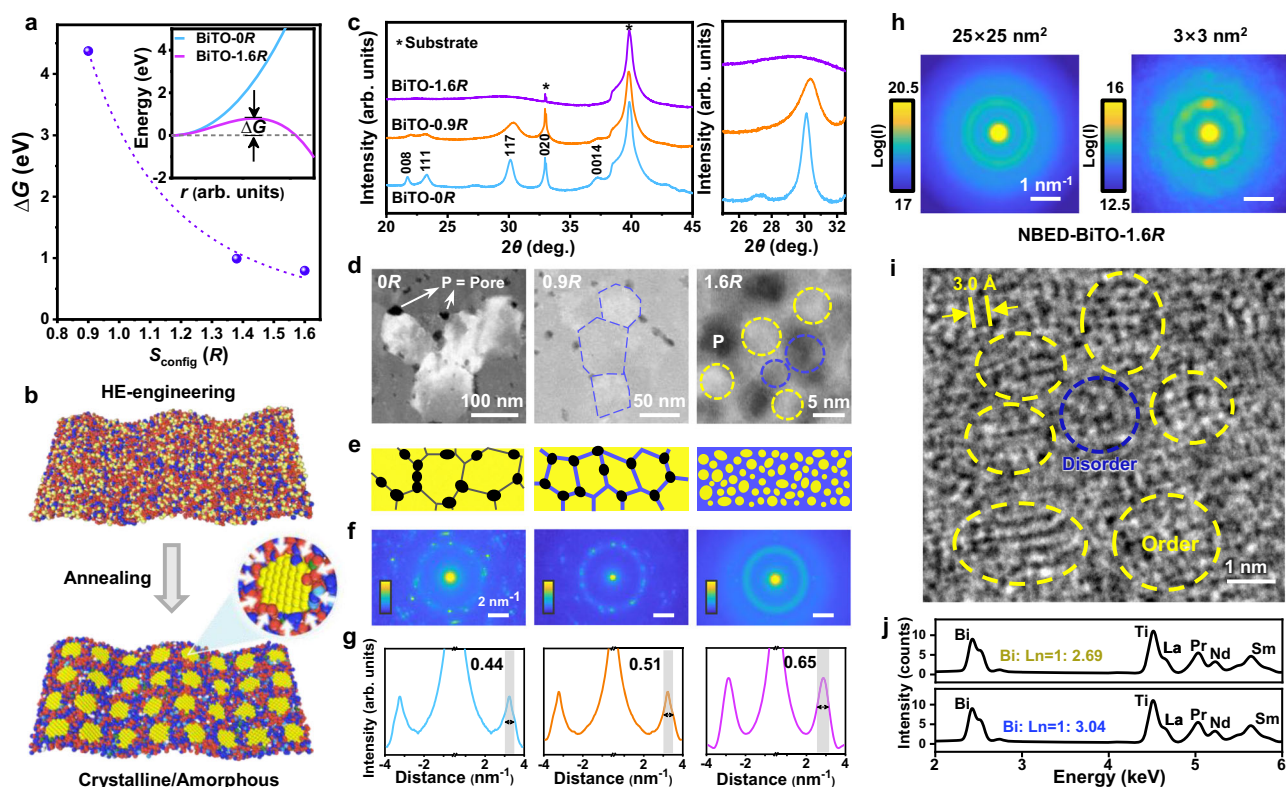


Fig. 1 | Implanting ordered structural motifs within an amorphous BiTO matrix via HE-engineering. **a** Calculated nucleation barrier (ΔG) for the amorphous phase as a function of configurational entropy in the BiTO system. The dashed curve is the non-linear fitting (Allometric 1 model) based on the data. Inset: Free energy changes as a function of the amorphous nucleus radius for the BiTO-0R, and BiTO-1.6R models. **b** Structural order modulation through a HE-engineering strategy: compositional fluctuation allows a spontaneous phase separation within a homogeneous ceramic base, with a medium-entropy nanophase approaching crystallization and a high-entropy nanophase staying at amorphous stages due to its sluggish crystallization kinetics, which results in a finely interconnected crystalline/amorphous microstructure. In the schematic diagram, Bi atoms are marked in both indigo-blue and yellow hues, while Ti, Nd, Pr, La, and Sm atoms are rendered in red,

white, sky blue, cyan-blue, and green, respectively. **c–f** XRD patterns (**c**), annular dark-field images (**d**), corresponding microstructural schematics (**e**) and electron diffraction analysis (**f**) of HE-engineered films. 0R and 0.9R: polycrystalline structures; thin amorphous films emerge in the grain boundaries of 0.9R (Supplementary Figs. 4 and 5). 1.6R: Nanocrystals embedded with an amorphous matrix. Illustrations: Yellow: crystalline BiTO; Blue: amorphous phase. Color bar in this figure (**f**): Normalize diffraction intensity. **g** Rotational averaged diffraction intensities integrated from the origin of reciprocal space to the {117} spots. **h** NBED patterns of the BiTO-1.6R film recorded in a 4D-STEM, integrated from regions of $25 \times 25 \text{ nm}^2$ and $3 \times 3 \text{ nm}^2$ in real space. The color bar is the log scale of intensity. **i** High-resolution IDPC image showing the crystalline/amorphous structure. **j** EDS spectra recorded from crystalline and amorphous regions.

integrated differential phase contrast (iDPC) imaging (Fig. 1i and Supplementary Fig. 9). Notably, the crystalline nanophase has a slightly high content of Bi element (molar ratio, Bi: Ln = 1: 2.69, deviating from the $x = 0.75$ composition), which gives a bright HAADF contrast and the dark one shows a high-entropy feature (Bi: Ln = 1: 3.04, near the equimolar region), as confirmed by quantitative energy-dispersive X-ray spectroscopy (EDS) analysis (Fig. 1j) and transmission electron microscopy equipped with energy-dispersive spectroscopy (TEM-EDS) mapping (Supplementary Fig. 10). The compositional undulation is indicative of spinodal-like phase separation³⁸ during the thermal processing of an amorphous film, allowing a composition with higher atomic mobilities (lower in configurational entropy) to initialize crystallization while after a certain time, forcing the remnant high-entropy counterpart to stabilize at amorphous stages owing to its sluggish crystallization nature. This picture aligns well with our HE-engineering strategy, generating regular fluctuations of structural order and chemical composition homogeneously over nanoscales.

Mechanical properties of the BiTO films

The finely modulated crystalline/amorphous microstructure might help to yield a certain level of flexibility that is unattained in conventional crystalline BiTO materials. To substantiate the beneficial effect of this structural design on mechanical properties, we conducted in-situ scanning electron microscopy (SEM) bending and transmission electron microscopy (TEM) tensile tests on HE-engineered BiTO samples. The results show that the BiTO-0.9R sample exhibits a typical brittle behavior, fracturing immediately when subjected to a bending load (Supplementary Fig. 11). The brittle nature is closely related to its microstructure, characterized by a substantial distribution of pores at the grain boundaries (Fig. 1d). These grain boundaries, along with the pores, could facilitate rapid crack propagation and result in intergranular fracture under deformation³⁹. As the configurational entropy increases, the BiTO-0.9R film exhibits a certain bending capability

before rupture (Fig. 2a and Supplementary Movie 1). Further finite element analysis (FEA) of bending states revealed that this film could sustain a maximum principal strain of about 0.80% (Fig. 2b and Supplementary Movie 2), which could be attributed to a reduction in both the size and the density of pores within the grain boundaries. The HE-engineered film (BiTO-1.6R) displays exceptional deformability, withstanding -180° bending without structural failure (Fig. 2c and Supplementary Movie 3). Corresponding FEA simulation suggests a maximum principal strain of up to 4.80% (Fig. 2d and Supplementary Movie 4). After this, a series of additional bending tests were conducted to test the flexibility of the BiTO-1.6R film. Under a bending strain of 1.50%, the film could revert to its original shape rapidly without suffering observable deformation (Supplementary Fig. 12 and Supplementary Movie 5), and it displayed remarkable resilience sustaining repetitive bending cycles (Supplementary Movie 6) as well.

In-situ TEM tensile loading experiments were further devised to mimic the response of thin film to stretching, a common stress state for flexible devices during service. As illustrated in Fig. 2e, when subjected to uniaxial tensile stress, the dog-bone-shaped BiTO-1.6R specimen underwent gradual elongation in length and finally ruptured with a maximum tensile elongation of 5.29%. The sample shows an almost linear elastic response according to the engineering stress-strain curve (Fig. 2f). Combined, our in-situ bending and tensile tests provide compelling evidence that the HE-engineering strategy provides an effective means to mitigate the inherent brittleness in the BiTO ceramic and endows it with exceptional flexibility.

Origin of the flexibility of high-entropy BiTO films

We then elucidate the root cause of the flexibility in the BiTO-1.6R film at a microscopic level. The contribution from the amorphous skeleton assembled from disordered motifs was first considered. For ease of calculation, AIMD simulations based on an amorphous model were performed to analyze the bonding structure evolution as a function of

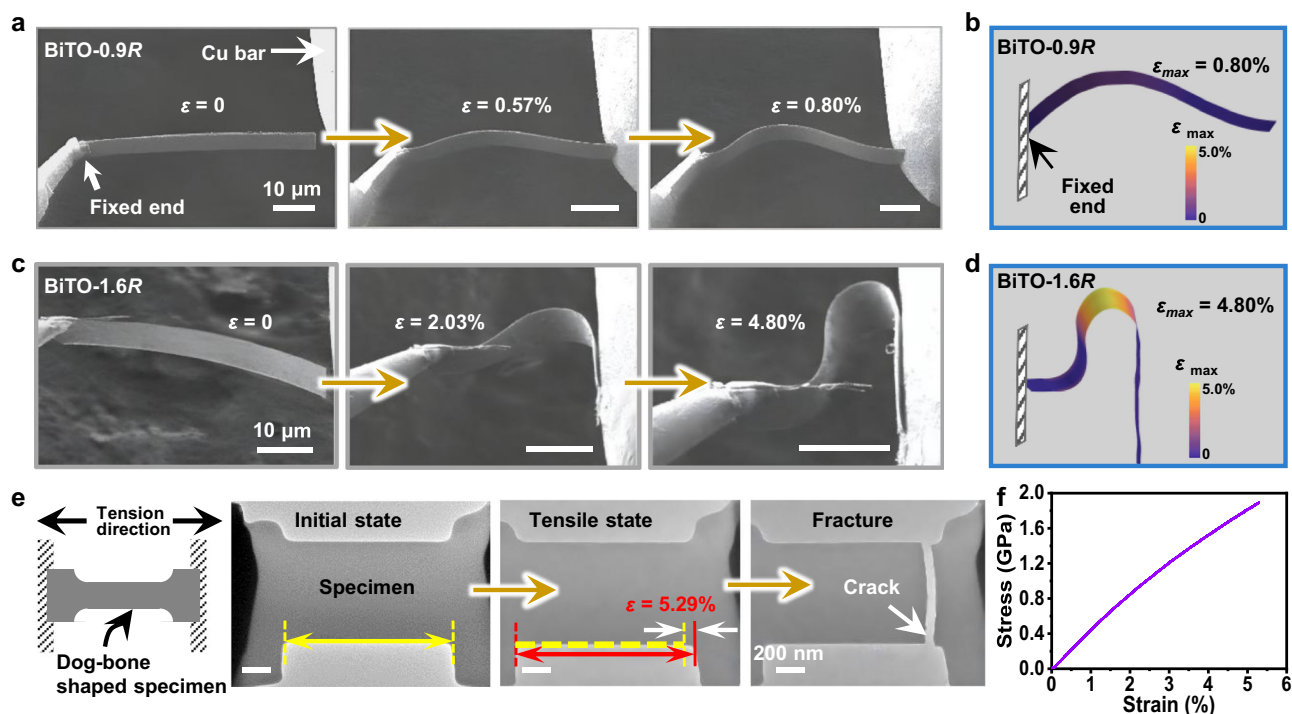


Fig. 2 | In-situ bending and tensile tests of entropy-modulated BiTO films. **a** Series of SEM images showing the bending process of a BiTO-0.9R film (sample size: $59 \mu\text{m} \times 5 \mu\text{m} \times 400 \text{nm}$). **b** The maximum bending strain derived from FEA simulation for the in-situ bending test of the BiTO-0.9R film. **c** Series of SEM images depicting the bending process of the BiTO-1.6R film (sample size: $50 \mu\text{m} \times 8 \mu\text{m} \times$

400nm). **d** The maximum bending strain derived from FEA for the BiTO-1.6R film. **e** Schematic of experimental setups of in-situ tensile loading conducted on the high entropy film (TEM images, BiTO-1.6R), yielding a maximum tensile strain of 5.29%. **f** Stress-strain curve of the BiTO-1.6R sample measured during the in-situ tensile test.

the imposed tensile strain (Fig. 3a and Supplementary Fig. 13). Compared with the undeformed state ($\epsilon = 0\%$, Supplementary Fig. 13), the calculated volumetric strain map under a 7.50% tensile strain (Fig. 3a) suggests a marked change in bond length during deformation. A localized increase in shear strain is further observed in the deformed states (Fig. 3a), indicating that the structural adaptivity is mediated by changes in the lengths and angles of bonds, as visualized in Fig. 3b and Supplementary Movie 7.

This structurally adaptive response to deformation is further supported by the precession electron diffraction (PED) measured under a series of strain states during in-situ tension testing (undeformed, tensile deformed at 2.10% and 4.08%). All the PED patterns were recorded from the same circular region ($r = 160$ nm) for ease of comparison. Detailed analysis of the PED data allows a meticulous assessment of the changes of atomistic structures under loading conditions, through a processed pair distribution function $G(r)$ that describes the probability of finding pairs of atoms as a function of the distance from a reference atom (r). As illustrated in Fig. 3c, the comparative $G(r)$ profiles reveal that the peak positions of the first to the fourth nearest neighbors of $G(r)$ at $\epsilon = 2.10\%$ and $\epsilon = 0\%$ exhibit minimal disparity, with minor variations in peak intensities. This suggests that the bonds tend to rotate when subjected to external strains. Upon increasing the strain to 4.08%, the first peak position, associated with the M (Metal = Bi, Ln, and Ti)-O bond lengths, shows minimal changes at peaks less than ~ 3 Å, while peaks broadening emerge around 3.7 Å (second-nearest neighbor distances through M-O-M bonds) and peak bifurcation was found near 5.5 Å. These facts suggest the cooperative rotations of TiO_6 octahedra or Bi/LnO_8 dodecahedra as a complete

structural unit. Our AIMD simulations and experimental $G(r)$ observations demonstrate that an amorphous matrix consisting of disordered motifs has more degrees of freedom to tolerate cooperative bond rotations, contributing to a primary flexibility in the BiTO-1.6R sample.

We note that, crystalline BiTO motifs tended to rotate under electron beam illumination, reflecting by changes in time-lapse Fast Fourier Transform patterns (Supplementary Fig. 14). It is indicative of electrostatic interactions between functional nanocrystals and the electron beam. Further, it led us to envisage that, BiTO crystals, as a typical piezoelectric material (Supplementary Fig. 15), may manifest a new structural adaptivity to strengthen flexibility, i.e., mass transport occurs to heal structural flaws as driven by internal electrical fields generated through stresses in the film, which are beyond the conventional knowledge of functional ceramics. To test our hypothesis, a two-step validation approach is required at electron-beam-off conditions (Fig. 3d): initially, the electrical response of BiTO nanocrystals needs to be established (biasing setup); subsequently, the mechanical plucking response of nanocrystals should be validated (plucking setup).

In terms of the electrical response, a bias voltage (5 V) was found to expedite the mass transport of functional crystals with a bright contrast (Fig. 3e). Interestingly, it was observed that mass migration is mainly spotted for functional crystals, leaving the amorphous substrate intact. This implicitly suggests that functional nanocrystals exhibit swift electrical responses while the adjacent amorphous matrix has a slow electrical response. The mechanical response of functional nanocrystals via a piezoelectric effect, if any, is expected to be detected within heavily deformed regions. An in-situ mechanical plucking

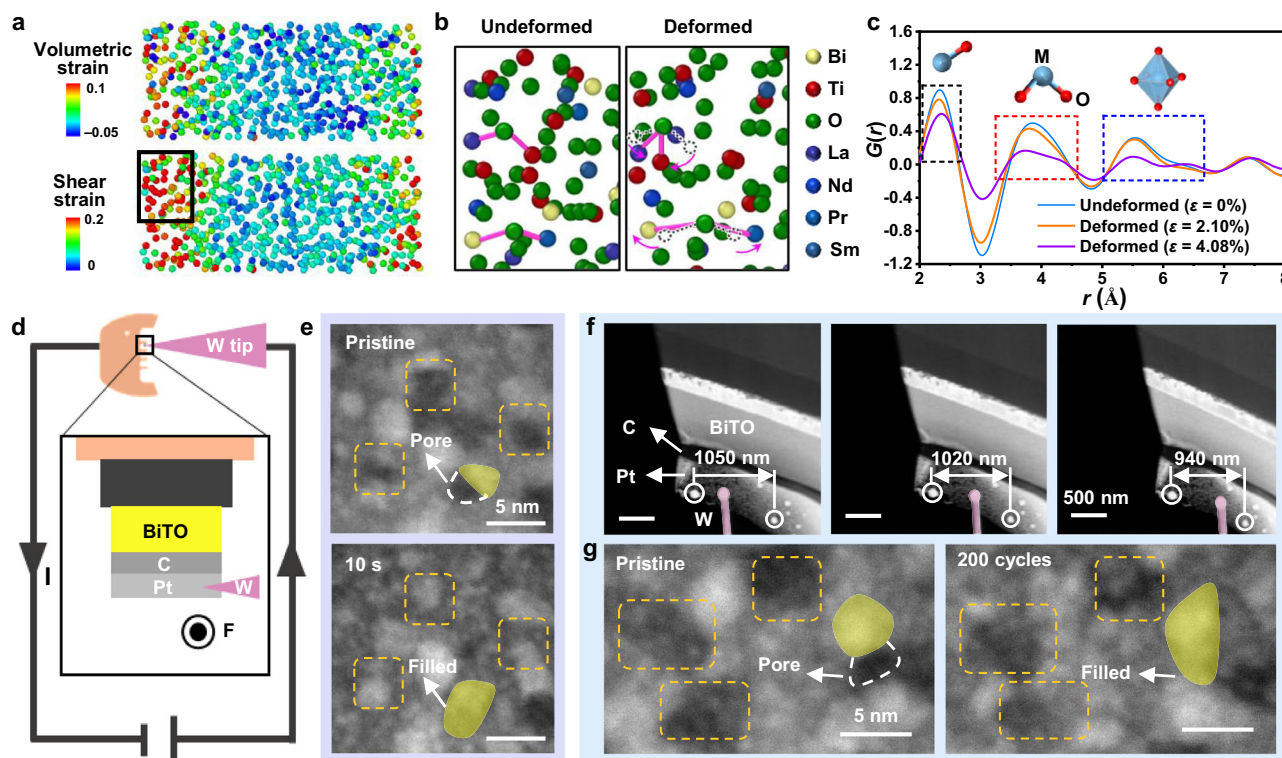


Fig. 3 | The origin of flexibility in BiTO-1.6R high-entropy films: contributions from amorphous motifs and functional nanocrystals. **a** Calculated volumetric strain map and shear strain map from an amorphous model after tensile deformation (7.5% tensile strain). The amorphous model has a S_{config} identical to that of the BiTO-1.6R sample. **b** Comparison of the atomic configuration from an identical region (black box region marked in (a)) before and after deformation. **c** Experimental $G(r)$ from the undeformed, 2.10%, and 4.08% tensile deformed BiTO-1.6R samples. **d** In-situ biasing and plucking setup designed to probe the

electrical and mechanical response of BiTO-1.6R films. **e** HAADF image pairs showing the evolution of BiTO nanocrystals subjected to electrical biasing, during which the electron beam was off. **f** STEM snapshots showing the cyclic plucking of BiTO-1.6 thin films by a W-needle. White circles were reference particles used to track the plucking process. **g** HAADF images acquired from identical regions before and after plucking, revealing the migration of BiTO crystals driven by mechanical forces.

experiment is devised to snapshot such localized interactions. This is proceeded by setting the plucking path of a W-needle at a certain fixed range under illumination, followed by 200 repeated loading cycles with the E-beam blanked (Fig. 3f and Supplementary Movie 8). After the experiment, we compared tens of reference regions scattered in the film, searching for a certain stress-concentrated region where migration of functional nanocrystals is observable. According to our experimental results, a minor share (3/10) showed detectable migration of functional BiTO nanocrystals (Fig. 3g). Overall, our elaborated TEM analyses suggest that local stress concentration, which is believed to trigger catastrophic crack propagation and deteriorate mechanical behaviors, could be employed as an effective energy input to activate the migration of functional nanocrystals. Then, they might be forced to infiltrate into the stress-concentrated crack tip, alleviating stress concentrations and possibly leading to crack deflection, which combines to contribute to new defect-healing flexibility via leverage of the piezoelectric effect.

Dielectric and optical properties of flexible high-entropy films

The microstructural design following our HE-engineering strategy is suitable for the creation of flexible functional ceramic devices. Capacitor devices using HE-engineered films were prepared to evaluate their overall performances, including flexibility, room-temperature permittivity, temperature-dependence permittivity, and transparency

(detailed in the “Methods”). Pertaining to our primary concern on flexibility, the results show that, the dielectric capacitor exhibits excellent bending stability after 1000 cycles with minimal variations of permittivity ($\leq 2.4\%$ at 1000 kHz, Fig. 4a and Supplementary Movie 9). A slight increase in permittivity is even observed at 1000 kHz after cyclic bending, which possibly implies a crack healing capacity of the capacitor. More importantly, a remarkable permittivity of ~ 35 is achieved at ambient temperature, which is superior to those obtained in organic and amorphous flexible dielectrics, e.g., the permittivity of PVDF/BaTiO₃ nanocomposites rested below 25⁴⁰. In addition, the high permittivity and low dielectric loss tangent (≤ 0.1) can be maintained over a broad temperature range from -100 to 200 °C (Fig. 4b), demonstrating a good temperature stability superior to those polymer-based dielectrics (Supplementary Fig. 16), thus rendering them promising for applications under extreme conditions, including cryogenic outer space environments and high-power heat-generating semiconductor devices. Moreover, enhanced insulation performance of the high-entropy dielectric capacitor was attained when compared to capacitors fabricated using 0R or 0.9R dielectric film (Fig. 4c). The leakage current density undergoes a pronounced decline from 3.6×10^{-2} A cm⁻² (BiTO-0R) to 3.2×10^{-7} A cm⁻² (BiTO-1.6R) at an electric field of 1.0 MV cm⁻¹, which is reasonably attributed to the presence of an interconnected high-entropy amorphous substrate with insulating properties.

The interconnected crystalline/amorphous structure design brings forth additional optical performance, as revealed by our

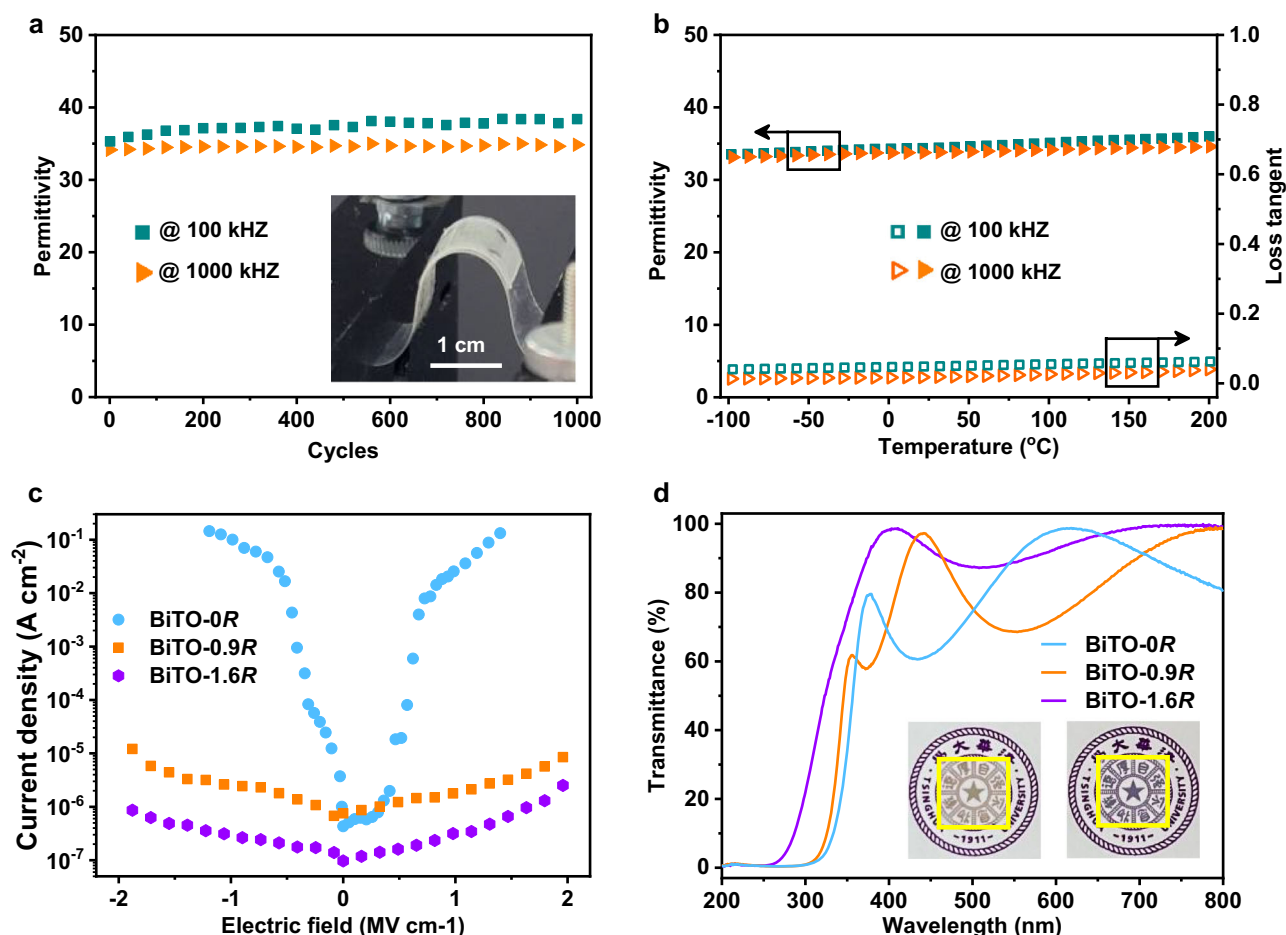


Fig. 4 | Dielectric and optical performance of the films. a Room-temperature permittivity of the high-entropy dielectric capacitor (BiTO-1.6R) as a function of bending cycles under tensile stress (frequency: 100 kHz and 1000 kHz). Bending radius: 3 mm. Inset: photograph of a flexible capacitor. **b** Temperature-dependent permittivity and loss tangent of the high-entropy film. **c** Leakage current densities

of the dielectric films as a function of applied electric fields. **d** Transmittance spectra of the films in the UV-visible light region. Inset: Digital photographs of BiTO-0.9R (left, near transparent) and BiTO-1.6R (right, transparent) films outlined by yellow frames.

experimental transmittance measurements (Fig. 4d). Pristine BiTO films ($x=0.00$, BiTO-OR) show evident absorption peaks at 377 nm, arising from the interbond absorption of $\text{Bi}_4\text{Ti}_3\text{O}_{12}$ -based bulk materials⁴¹. A substitution of Bi with Ln in BiTO crystals ($x=0.25$, BiTO-0.9R) shifted the interbond absorption peaks to ~443 nm. In the HE-engineered film ($x=0.75$), a decrease in the content of nanocrystals lowers their absorption capacity, and full elimination of grain boundaries and pores also reduces the multiple reflections or interferences (>475 nm)⁴² between the film and the substrate. Together, they yield an experimental transmittance of over 90% within the visible light range, behaving like transparent glass ceramics^{43,44}. Given the excellent dielectric performance and the high optical transmittance of our flexible capacitor (Fig. 4d, inset), our high-entropy ceramic film exhibits considerable potential for next-generation flexible displays and touch panels.

Discussion

We demonstrated an entropy strategy to effectively modulate the nanoscale undulation of structural order in functional ceramics, thus resulting in a finely modulated crystalline/amorphous microstructure. This ideal mosaic microstructure efficiently integrates mechanical flexibility with functionalities in a $\text{Bi}_3\text{Ti}_4\text{O}_{12}$ -based ceramic, leading to the successful fabrication of a thick (>400 nm), yet exceptionally flexible and transparent, dielectric capacitor devices with high permittivity and durability. Our work provides a broadly applicable paradigm for realizing mechanical flexibility in functional ceramics with a wide property spectrum. Moreover, new physics may emerge in this mosaic structure, especially from the intimate interaction between ordered and disordered motifs. We propose that it will foster fascinating and unexpected properties beyond flexibility, such as optical transparency, high-temperature stability, corrosion resistance, etc.

Methods

Sample preparation

The entropy-modulated films were deposited on substrates using a chemical solution deposition (CSD) method, which is simple, efficient, and cost-effective. Precursor solutions for deposition were prepared by dissolving high-purity raw precursor reagents (bismuth acetate, lanthanum acetate, praseodymium acetate, neodymium acetate, samarium acetate, and tetrabutyl titanate) in propionic acid at 60 °C for 10 min. The cation concentrations of the solutions were controlled to be 0.1 mol L⁻¹ with a 5% excess of bismuth acetate to compensate for the volatilization of Bi during the heat treatment. The obtained precursor solutions were further filtered through syringe filters with a pore size of 0.22 μm to remove possible impurities, thus obtaining clear and transparent solutions for CSD.

In this work, two types of substrates were used for the deposition of the prepared precursor solutions. The target films for the mechanical tests of the freestanding films were deposited on Au (protective layer)/ $\text{Sr}_3\text{Al}_2\text{O}_6$ (SAO, sacrificial layer)/ SrTiO_3 (STO) substrates. The spin rate for CSD was 6000 rpm and the spin time was 20 s, followed by pyrolysis (150 °C for 2 min and 400 °C for 10 min) and rapid thermal annealing process (600 °C for 30 min). The films were then stripped from the rigid substrate by covering the film with a polydimethylsiloxane membrane and dissolving the sacrificial layer (SAO) in deionized water at room temperature. The all-inorganic flexible capacitors were fabricated using fluorophlogopite as substrate. The solution deposition parameters, drying process, and thermal annealing process for the entropy-modulated films on the two substrates are the same.

The SAO (thickness: ~60 nm) was grown on STO (001) substrates using pulsed laser deposition in the oxygen partial pressures of 1×10^{-6} Torr. All STO substrates were TiO_2 -terminated, which were achieved by aqua regia etching and then 950 °C annealing in air. The target was sintered polycrystalline SAO pallet (Hefei Kejing Material Technology

Co., Ltd.), and was ablated by an excimer laser ($\lambda=248$ nm) with a repetition rate of 2 Hz and a laser fluence of 1.8 J cm⁻². During the growth, the STO substrates were kept at 760 °C. All samples were cooled down to room temperature in the pressure of 1×10^{-6} Torr⁴⁵. The Au layer (thickness: ~10 nm) was deposited onto SAO/STO substrate through a ion sputtering instrument (SBC-12, Chengdu Zhongke Wish Instruments Co.,Ltd.), to protect the SAO layer from sol damage during spin coating process.

Characterizations

We characterized the crystal structures of prepared films by an X-ray diffractometer (Smartlab, Rigaku) with Cu-K α radiation ($\lambda=1.5418$ Å). The surface morphology and thickness of the films were characterized by field emission scanning electron microscopy (MERLIN VP Compact, ZEISS). The bending test of the freestanding films was performed in a focused ion beam scanning electron microscope (Crossbeam 340, ZEISS) system, which includes a nanomanipulator and a Cu bar. In-situ tensile test was performed by welding the sample to a push-to-pull device and applying a uniaxial tensile load to the device.

Thin lamellae for TEM/STEM characterization were extracted using a Helios G4 CX FIB system (Thermo Fisher Scientific). The samples were thinned down to 50 nm using an accelerating voltage of 30 kV with a decreasing current from 240 pA to 50 pA, followed by a fine and careful low-kV polishing (5 kV, 20 pA) to reduce beam-induced damage or sample decomposition. Bright-field, low-magnified HAADF, along with high-resolution TEM (HRTEM) images, and electron diffraction patterns were captured through a Thermo Fisher Scientific Talos F200s TEM (200 kV) under low-beam currents to minimize beam damage. Atomic-resolution integrated Differential Phase Contrast (iDPC) and HAADF imaging were conducted on a Thermo Fisher Scientific Themis Z AC-STEM (300 kV), where energy-dispersive X-ray spectroscopy (EDS) spectra were acquired from interested regions as well. In-situ TEM experiment was performed within a Thermo Fisher Scientific Talos F200s TEM (200 kV), utilizing a TEM-scanning tunneling microscope sample holder (ZepTools Co., Ltd., China). A relative bias of 5 V was employed during the electrical biasing process.

The 4D-STEM was performed on a Titan Cubed Themis (Thermo Fisher Scientific, operated at 300 kV with a probe-forming semi-angle of 1.2 mrad), equipped with a high brightness electron gun (X-FEG with monochromator). 4D-STEM datasets were acquired with 1 ms acquisition time (with an additional 0.86 ms readout time) per diffraction, 0.4 nm scan step, 256 × 256 scan points for each dataset, and a beam current of 80 pA. The nominal camera length is 1.15 m. HAADF image is acquired with 25 mrad probe-forming semi-angle and 48 - 200 mrad collection angle.

Au top electrodes (with diameters of ~150 μm and thickness of ~100 nm) were deposited onto the film (use the same ion sputtering instrument used for deposition Au layer on the SAO), to characterize the electrical properties of the films and devices. The precision impedance analyzer (HP 4294 A, Agilent) was used to obtain the permittivity and loss tangent over a broad frequency (1 kHz to 1000 kHz) and temperature range (-100 °C to 200 °C) with an AC voltage of 0.5 V. The leakage current properties were measured on a Sawyer-Tower circuit (Precision Multiferroic II, Radiant Technologies). The transmittance spectra of the films were characterized by UV/Vis/NIR spectrophotometer spectrophotometer (LAMBDA1050+, PerkinElmer Inc.).

Thermodynamic calculations of the films

AIMD simulations were conducted using CP2K package⁴⁶. The Perdew-Burke-Ernzerhof functional⁴⁷ and Goedecker-Teter-Hutter pseudopotentials⁴⁸ were employed. A plane-wave basis set was adopted with an energy cutoff of 400 Ry and 40 Ry for the finest level of a multi-grid and a reference grid covered by a Gaussian with unit

standard deviation, respectively. Periodic supercells of Bi₄Ti₃O₁₂ containing 684 atoms were used. The crystalline atomistic models with x of 0.25, 0.50, and 0.75 were created by randomly substituting Bi atoms with La, Nd, Pr, and Sm atoms, followed by isothermal-isobaric annealing at 300 K for 5 ps, so that the crystalline models were fully equilibrated. To create the amorphous counterparts, the equilibrated crystalline models were heated to 3500 K and held for 2 ps. Then, the models were quenched to 300 K in 3 ps and then equilibrated at 300 K for 12 ps so that the amorphous models were fully relaxed (Supplementary Fig. 1).

According to the classical nucleation theory, the free energy change (W) for the formation of a spherical amorphous nucleus with radius of r is calculated by the Eq. (2):

$$W(r) = \frac{4\pi r^3}{3} (f_{\text{amor}} - f_{\text{crys}}) + 4\pi r^2 \gamma \quad (2)$$

where f_{amor} , f_{crys} are the free energy densities of the amorphous phase and the crystalline phases, respectively, and γ is the crystalline-amorphous interfacial energy (herein, the γ is set as 1 J/m²). We calculated both f_{amor} and f_{crys} at different values of S_{config} . The results show that the $f_{\text{amor}} - f_{\text{crys}}$ decrease significantly with increasing S_{config} . (Supplementary Fig. 2a). On this basis, the W of the different films as a function of r was obtained (Supplementary Fig. 2b). Further, the nucleation rate K is limited by the free energy barrier (ΔG , the maximum of $W(r)$) as the Eqs. (3) and (4):

$$\Delta G = \frac{16\pi\gamma^3}{3(f_{\text{amor}} - f_{\text{crys}})^2} \quad (3)$$

$$K \propto \exp\left(-\frac{\Delta G}{k_B T}\right) \quad (4)$$

As shown in Fig. 1a, the energy barrier ΔG reduces as the configuration entropy increases. This results in a rapid rise in the nucleation rate of the amorphous phase. Consequently, increased entropy results in a greater proportion of the amorphous phase, as evidenced by our observations in HRTEM analyses.

Finite element analyses (FEA) of films

We performed FEA using ABAQUS (version 6.11) to probe the strain fields in two films (BiTO-0.9R and BiTO-1.6R) in the in-situ SEM bending tests. Two shell models were created according to the measured dimensions of the two films in SEM images: the size of the models corresponds to the samples used for mechanical testing (50 $\mu\text{m} \times 8 \mu\text{m} \times 400 \text{ nm}$ for BiTO-1.6R and 59 $\mu\text{m} \times 5 \mu\text{m} \times 400 \text{ nm}$ for BiTO-0.9R). Four-node reduced-integration shell elements with an average mesh size of 0.2 $\mu\text{m} \times 0.2 \mu\text{m}$ were used to mesh the models. Isotropic elastic constitutive behavior was assigned to simulate both films. The elastic moduli of 70 GPa and 122 GPa were used for the films of BiTO-1.6R and BiTO-0.9R, respectively. A Poisson's ratio of 0.24 was used for both films⁴⁹.

Uniaxial strain tensile simulation

Uniaxial strain tensile tests were performed on the amorphous BiTO-1.6R (Supplementary Fig. 1) model at 300 K by modifying the CP2K code according to ref. 50. The nominal strain rate of 0.3 ps⁻¹ and a timestep of 1 fs were used.

The precession electron diffraction (PED) measurement

The PED measurements were performed using a JEM-ARM300F2 (JEOL Ltd.), equipped with a OneView camera. The tensile loading was conducted by using an in situ Bestron-TEM holder. The accelerating voltage was 300 kV and the distance from the sample to detector is

800 mm. The precession angle was 0.9° for the sample and exposure time was 1 s. Data analysis was performed using EPDF SUITE software (ECM29, ePDFWorkshop, Croatia).

Statistics and reproducibility

The experiments in this paper were repeated at least three times.

Reporting summary

Further information on research design is available in the Nature Portfolio Reporting Summary linked to this article.

Data availability

All data generated in this study are provided with this paper. The source data used in this study have been deposited in the Figshare database under accession code <https://doi.org/10.6084/m9.figshare.28830788>. Source data are provided with this paper.

References

1. Yin, Q. R., Zhu, B. H. & Zeng, H. R. *Microstructure, Property and Processing of Functional Ceramics* (Springer, 2010).
2. Saito, Y. et al. Lead-free piezoceramics. *Nature* **432**, 84–87 (2004).
3. Lemons, J. E. Ceramics: past, present, and future. *Bone* **19**, S121–S128 (1996).
4. Cooper, C. B. et al. Autonomous alignment and healing in multilayer soft electronics using immiscible dynamic polymers. *Science* **380**, 935–941 (2023).
5. Pan, H. et al. Ultrahigh energy storage in superparaelectric relaxor ferroelectrics. *Science* **374**, 100–104 (2021).
6. Zhao, Z. Y., Liu, K., Liu, Y. W., Guo, Y. L. & Liu, Y. Q. Intrinsically flexible displays: key materials and devices. *Natl. Sci. Rev.* **9**, nwac090 (2022).
7. Xie, J. Y. et al. Highly foldable, super-sensitive, and transparent nanocellulose/ceramic/polymer cover windows for flexible OLED displays. *ACS Appl. Mater. Interfaces* **14**, 16658–16668 (2022).
8. Yu, J. C. et al. Ultralow thermal conductivity and high ZT of Cu₂Se-based thermoelectric materials mediated by TiO₂-n nanoclusters. *Joule* **8**, 1–15 (2024).
9. Zhang, M. et al. Ultrahigh energy storage in high-entropy ceramic capacitors with polymorphic relaxor phase. *Science* **384**, 185–189 (2024).
10. Gao, W. X., Zhu, Y., Wang, Y. J., Yuan, G. L. & Liu, J.-M. A review of flexible perovskite oxide ferroelectric films and their application. *J. Materiomics* **6**, 1–16 (2020).
11. Bretos, I. et al. Activated solutions enabling low-temperature processing of functional ferroelectric oxides for flexible electronics. *Adv. Mater.* **26**, 1405–1409 (2014).
12. Won, S. S. et al. Flexible vibrational energy harvesting devices using strain-engineered perovskite piezoelectric thin films. *Nano Energy* **55**, 182–192 (2019).
13. Liang, Z. S. et al. All-inorganic flexible embedded thin-film capacitors for dielectric energy storage with high performance. *ACS Appl. Mater. & Interfaces* **11**, 5247–5255 (2019).
14. Liang, Z. S. et al. Flexible lead-free oxide film capacitors with ultrahigh energy storage performances in extremely wide operating temperature. *Nano Energy* **57**, 519–527 (2019).
15. Wu, Y. J. et al. Twisted-layer boron nitride ceramic with high deformability and strength. *Nature* **626**, 779–784 (2024).
16. Xu, X. et al. Double-negative-index ceramic aerogels for thermal superinsulation. *Science* **363**, 723–727 (2019).
17. Meza, L. R., Das, S. & Greer, J. R. Strong, lightweight, and recoverable three-dimensional ceramic nanolattices. *Science* **345**, 1322–1326 (2014).
18. Xu, Z. et al. Inhibited grain growth through phase transition modulation enables excellent mechanical properties in oxide ceramic nanofibers up to 1700 °C. *Adv. Mater.* **35**, 2305336 (2023).

19. Li, L. et al. Nanograin-glass dual-phasic, elasto-flexible, fatigue-tolerant, and heat-insulating ceramic sponges at large scales. *Mater. Today* **54**, 72–82 (2022).
20. Zhang, J. et al. Plastic deformation in silicon nitride ceramics via bond switching at coherent interfaces. *Science* **378**, 371–376 (2022).
21. Dong, L. R. et al. Borrowed dislocations for ductility in ceramics. *Science* **385**, 422–427 (2024).
22. Tian, Y. J. et al. Ultrahard nanotwinned cubic boron nitride. *Nature* **493**, 385–388 (2013).
23. Guo, J. R. et al. Hypocrystalline ceramic aerogels for thermal insulation at extreme conditions. *Nature* **606**, 909–916 (2022).
24. Hu, C. Z., Li, Y. W., Yu, Z. Y. & Luo, J. Computing grain boundary diagrams of thermodynamic and mechanical properties. *npj Comput. Mater.* **7**, 159 (2021).
25. Simonov, A. & Goodwin, A. L. Designing disorder into crystalline materials. *Nat. Rev. Chem.* **4**, 657–673 (2020).
26. Kao, K. C. *Dielectric Phenomena in Solids* (Elsevier, 2004).
27. Pelleg, J. *Mechanical Properties of Materials* (Springer, 2013).
28. Hong, S. S. et al. Extreme tensile strain states in $\text{La}_{0.7}\text{Ca}_{0.3}\text{MnO}_3$ membranes. *Science* **368**, 71–76 (2020).
29. Guo, Y. T. et al. Remarkable flexibility in freestanding single-crystalline antiferroelectric PbZrO_3 membranes. *Nat. Commun.* **15**, 4414 (2024).
30. Dong, G. H. et al. Super-elastic ferroelectric single-crystal membrane with continuous electric dipole rotation. *Science* **366**, 475–479 (2019).
31. Dong, J. et al. Non-affine atomic rearrangement of glasses through stress-induced structural anisotropy. *Nat. Phys.* **19**, 1896–1903 (2023).
32. Frankberg, E. J. et al. Highly ductile amorphous oxide at room temperature and high strain rate. *Science* **366**, 864–869 (2019).
33. Hays, C. C., Kim, C. P. & Johnson, W. L. Microstructure controlled shear band pattern formation and enhanced plasticity of bulk metallic glasses containing in situ formed ductile phase dendrite dispersions. *Phys. Rev. Lett.* **84**, 2901 (2000).
34. Wu, Y., Xiao, Y. H., Chen, G. L., Liu, C. T. & Lu, Z. P. Bulk metallic glass composites with transformation-mediated work-hardening and ductility. *Adv. Mater.* **25**, 2770–2773 (2010).
35. Doremus, R. H. Mixed-alkali effect and interdiffusion of Na and K ions in glass. *J. Am. Ceram. Soc.* **57**, 478–480 (1974).
36. Rost, C. M. et al. Entropy-stabilized oxides. *Nat. Commun.* **6**, 8485 (2015).
37. Sarkar, A. et al. High-entropy oxides: fundamental aspects and electrochemical properties. *Adv. Mater.* **31**, 1806236 (2019).
38. Porter, D. A. & Easterling, K. E. *Phase Transformations in Metals and Alloys (revised reprint)* (CRC Press, 2009).
39. Zarnas, P. D., Boyce, B. L., Qu, J. M. & Dingreville, R. Stress-induced transition from vacancy annihilation to void nucleation near microcracks. *Int. J. Solids Struct.* **213**, 103–110 (2021).
40. Zhou, T. et al. Improving dielectric properties of BaTiO_3 /ferroelectric polymer composites by employing surface hydroxylated BaTiO_3 nanoparticles. *ACS Appl. Mater. Interfaces* **3**, 2184–2188 (2011).
41. Bai, W. et al. Electrical, magnetic, and optical properties in multi-ferroic $\text{Bi}_5\text{Ti}_3\text{FeO}_{15}$ thin films prepared by a chemical solution deposition route. *J. Appl. Phys.* **109**, 6 (2011).
42. Bai, W. et al. Investigations on electrical, magnetic and optical behaviors of five-layered Aurivillius $\text{Bi}_6\text{Ti}_3\text{Fe}_2\text{O}_{18}$ polycrystalline films. *Thin Solid Films* **525**, 195–199 (2012).
43. Llordés, A., Garcia, G., Gazquez, J. & Milliron, D. J. Tunable near-infrared and visible-light transmittance in nanocrystal-in-glass composites. *Nature* **500**, 323–326 (2013).
44. Edgar, A., Williams, G. V. M. & Hamelin, J. Optical scattering in glass ceramics. *Curr. Appl. Phys.* **6**, 355–358 (2006).
45. Yang, A. J. et al. Multifunctional magnetic oxide- MoS_2 heterostructures on silicon. *Adv. Mater.* **35**, 2302620 (2023).
46. Kühne, T. D. et al. CP2K: an electronic structure and molecular dynamics software package-Quickstep: efficient and accurate electronic structure calculations. *J. Chem. Phys.* **152**, 19 (2020).
47. Perdew, J. P., Burke, K. & Ernzerhof, M. Generalized gradient approximation made simple. *Phys. Rev. Lett.* **77**, 3865–3868 (1996).
48. Goedecker, S., Teter, M. & Hutter, J. Separable dual-space Gaussian pseudopotentials. *Phys. Rev. B* **54**, 1703–1710 (1996).
49. Chen, Y. et al. Fracture behaviors and ferroelastic deformation in W/Cr Co-doped $\text{Bi}_4\text{Ti}_3\text{O}_{12}$ ceramics. *J. Am. Ceram. Soc.* **99**, 2103–2109 (2016).
50. Matusalem, F., Santos Rego, J. & de Koning, M. Plastic deformation of superionic water ices. *Proc. Natl. Acad. Sci. USA* **119**, e2203397119 (2022).

Acknowledgements

We thank Prof. W. Miao (Tsinghua University) and beamline scientists at BSRF-1W1A, BSRF-1W1B, and BSRF-4B7B beamlines (Institute of High Energy Physics) for fruitful discussions. This work was supported by the Basic Science Center Project of the National Natural Science Foundation of China (NSFC) (grant no. 52388201, Y.-H.L. and C.-W.N.), National Key Research Program of China (grant no. 2021YFB3800601, Y.-H.L.), the NSFC (grant no. 52102275, L.Y.D.; grant nos. 12474095 and 52402323, B.B.Y.; grant no. 12302077, W.Q.Z.; grant no. 12075273, W.X.; grant no. 12325203, X.Y.L.; grant nos. 52222102 and 22272024, Z.Y.Y., grant nos. 12325202 and 12172005, X.D.W.), the Fundamental Research Funds for the Central Universities (grant no. FRF-IDRY-23-034, L.Y.D.), the Hundred-Talent Program of Chinese Academy of Sciences (grant no. 2023000641, B.B.Y.), the Yunnan Fundamental Research Projects (grant nos. 202101BE070001-012 and 202201AT070171, L.W.). The numerical calculations in this study were carried out on the ORISE Supercomputer.

Author contributions

L.Y.D., B.B.Y., and Y.-H.L. conceived this study. L.Y.D., B.B.Y., and X.Y.Y. performed this study with the supervision of Y.-H.L., C.-W.N., X.D.W., and Z.Y.Y. L.Y.D. and B.B.Y., fabricated the samples and carried out characterizations with assistance from S.L., Y.Q.L., Q.L., Y.J.Z., and W.X. X.Y.Y., Y.Z., H.L.C., and Z.Y.Y., carried out the TEM and STEM analysis. W.Q.Z., Y.J.J., B.F., and X.D.W. conducted the FEA, DFT and AMID calculations. X.Z., S.C.L., X.Y.L., and P.H.L., carried out the mechanical tests. X.Y.Z., and L.W., fabricated the substrates with $\text{Sr}_3\text{Al}_2\text{O}_6$ sacrificial layer. L.Y.D., B.B.Y., and X.Y.Y., analyzed the data and wrote the first draft of the manuscript. All authors discussed the results and revised the manuscript.

Competing interests

The authors declare no competing interests.

Additional information

Supplementary information The online version contains supplementary material available at <https://doi.org/10.1038/s41467-025-60548-0>.

Correspondence and requests for materials should be addressed to Xiaoding Wei, Zhiyang Yu or Yuan-Hua Lin.

Peer review information *Nature Communications* thanks the anonymous, reviewer(s) for their contribution to the peer review of this work. A peer review file is available.

Reprints and permissions information is available at <http://www.nature.com/reprints>

Publisher's note Springer Nature remains neutral with regard to jurisdictional claims in published maps and institutional affiliations.

Open Access This article is licensed under a Creative Commons Attribution-NonCommercial-NoDerivatives 4.0 International License, which permits any non-commercial use, sharing, distribution and reproduction in any medium or format, as long as you give appropriate credit to the original author(s) and the source, provide a link to the Creative Commons licence, and indicate if you modified the licensed material. You do not have permission under this licence to share adapted material derived from this article or parts of it. The images or other third party material in this article are included in the article's Creative Commons licence, unless indicated otherwise in a credit line to the material. If material is not included in the article's Creative Commons licence and your intended use is not permitted by statutory regulation or exceeds the permitted use, you will need to obtain permission directly from the copyright holder. To view a copy of this licence, visit <http://creativecommons.org/licenses/by-nc-nd/4.0/>.

© The Author(s) 2025